Progress In Electromagnetics Research C, Vol. 154, 183–190, 2025

(Received 22 January 2025, Accepted 8 April 2025, Scheduled 12 April 2025)

SAF-SFT-SRAF-Based Signal Coherent Integration Method for High-Speed Target Detecting in Airborne Radar

Wenwen Xu, Yuhang Wang, Jidan Huang, Hao Wang, and Jianyin Cao*

School of Electronic and Optical Engineering, Nanjing University of Science and Technology, Nanjing 210094, China

ABSTRACT: In radar target detection, long-term coherent integration (LTCI) is widely employed to improve the signal-to-noise ratio (SNR) and enhance the detection capability for weak and small targets. Meanwhile, the airborne radar, with advantages of wide-area surveillance, high sensitivity, and strong maneuver ability, demonstrates significant superiority in detecting high-speed targets. However, during the flight of the airborne radar platform, motion errors and the relative motion of high-speed targets can cause significant range migration (RM) and Doppler frequency migration (DFM), degrading coherent integration performance. To this end, this paper proposes a coherent integration method for high-speed target in airborne radar based on the symmetric autocorrelation function, scaled Fourier transform, and sequence reversing autocorrelation function (SAF-SFT-SRAF). Detailed comparisons between SAF-SFT-SRAF and several typical methods demonstrate that the proposed method effectively balances computational complexity and detection performance.

1. INTRODUCTION

In radar target detection, long-term coherent integration (LTCI) is widely employed to improve the signal-to-noise ratio (SNR) and enhance the detection capability for weak targets [1–3]. However, during the coherent integration of uniformly accelerated targets, the motion of high-speed targets can induce both range migration (RM) and Doppler frequency migration (DFM), resulting in a significant degradation in coherent integration performance [4–6]. In actual airborne radar applications, the aircraft experiences significant external disturbances while flying in the atmosphere, causing it to deviate from the ideal straight-line motion and produce noticeable motion errors [7, 8], which further exacerbates the RM and DFM.

Currently, research on LTCI for uniformly accelerated motion is mainly divided into correction-compensation methods and search-integration methods. For correction-compensation methods, one approach first performs RM correction and treats the target echo as a linear frequency-modulated (LFM) signal within the slow-time domain, where acceleration is estimated based on the chirp rate of the LFM signal. Common methods for RM correction include keystone transform (KT) [9], scaled inverse Fourier transform (SCIFT) [10], symmetric autocorrelation function-scaled Fourier transform (SAF-SFT) [11], etc. Acceleration estimation methods include the second-order Wigner-Ville distribution (SoWVD) [12], Lv's distribution (LVD) [13], coherently integrated cubic phase function (CICPF) [14], etc. Another approach is to estimate motion parameters of targets simultaneously, such as three-dimensional scaled transform (TDST) [15] and three-dimensional coherent integration (TDCI) [16]. These methods have lower computational complexity than search-integration methods but have inferior anti-noise performance. Compared with the correction-compensation method, the search-integration method has better anti-noise performance and higher computational complexity. A representative method is the generalized Radon Fourier transform (GRFT) [17], which compensates the target trajectory and integrates echo energy by jointly searching for multiple motion parameters, providing strong anti-noise performance. However, the mechanism of traversal search leads to a substantial computational burden.

Motion error compensation for airborne radar primarily includes methods based on aircraft attitude and echo data. Aerial attitude-based compensation [18, 19] relies on motion parameters recorded by devices such as the inertial measurement unit (IMU) and global positioning system (GPS). In addition, the decoupling techniques are applied to the point-by-point compensation of two-dimensional space-variant errors. However, the performance is influenced by the accuracy of the devices and environmental interference. Echo-based compensation [20, 21] estimates errors by analyzing echo characteristics, with techniques such as image contrast optimization and waveform entropy minimization. However, under low SNR conditions, the difficulty in extracting echo characteristics can significantly reduce the accuracy of compensation.

Several improved methods have been proposed to address the impact of airborne platform motion errors on the coherent integration of echo signals from high-speed targets. These include the sequence reversing transform and special GRFT (SRT-SGRFT) [22] and the improved GRFT (IGRFT) [23]. The IGRFT method extends the GRFT by incorporating a search for platform motion errors, achieving coherent integration with strong anti-noise performance. However, the five-dimensional search mechanism results in high computational complexity, making it impractical for applications. SRT-SGRFT method re-

---

* Corresponding author: Jianyin Cao (jianyin.cao@njust.edu.cn).

doi:10.2528/PIERC25012202

Published by THE ELECTROMAGNETIC ACADEMY

duces the computational complexity by employing a hierarchical search strategy: first performing a two-dimensional search for range and acceleration, followed by a three-dimensional search for sinusoidal error parameters and velocity. Despite this optimization, the multi-dimensional search still has high computational complexity, leading to application limitations.

This paper proposes an sequence reversing autocorrelation function (SRAF) to estimate sinusoidal motion error parameters and combines it with the traditional SAF-SFT method to obtain SAF-SFT-SRAF method. First, the equivalent velocity between the target and radar is estimated using SAF-SFT operation, and the resulting compensation function corrects the RM caused by velocity. Next, after performing an SRAF operation, the sinusoidal motion error parameters are jointly estimated, enabling the correction of sinusoidal motion error. Finally, SAF-SFT operation is applied again to estimate the equivalent acceleration and construct a compensation function for DFM correction. Detailed experiments are provided to demonstrate the effectiveness of the proposed method. The results show that the proposed method achieves a good balance between computational complexity and detection performance.

The rest of this paper is organized as follows. In Section 2, a signal model considering motion errors is established. The proposed method is described in detail in Section 3. Then, some simulation results are provided in Section 4.

2. SIGNAL MODEL

The chirp signal emitted by the radar can be expressed as

$$S_t(t) = \text{rect}\left(\frac{t}{T_p}\right)\exp\left(j2\pi f_c t + j\pi\mu t^2\right), \tag{1}$$

where $\text{rect}\left(\frac{t}{T_p}\right) = \left\{\begin{array}{ll} 1, & |t| \le T_p/2 \\ 0, & |t| > T_p/2 \end{array}\right.$, t is the fast time, f_c the carrier frequency, T_p the pulse width, and μ the frequency modulation.

After down conversion, the received echo signal can be expressed as

$$S_r(t, t_m) = A_r \text{rect}\left\{\frac{[t - 2R(t_m)/c]}{T_p}\right\}\exp\left[-\text{j}\frac{4\pi f_c}{c}R(t_m)\right] \times \exp\left\{\text{j}\pi\mu\left[t - \frac{2R(t_m)}{c}\right]^2\right\}, \tag{2}$$

where A_r is the amplitude of the received signal, c the light speed, $R(t_m)$ the radial distance between the target and the radar, $t_m = mT_r$ the slow time, T_r the pulse repetition time (PRT), $m = -M/2, \ldots, M/2$ the transmitted pulse number index, and M the number of coherent integrated pulses, assumed to be even.

After pulse compression (PC), the result is given by

$$S_p(t, t_m) = A\text{sinc}\left\{B\left[t - \frac{2R(t_m)}{c}\right]\right\}\exp\left[-\text{j}\frac{4\pi}{\lambda}R(t_m)\right], \tag{3}$$

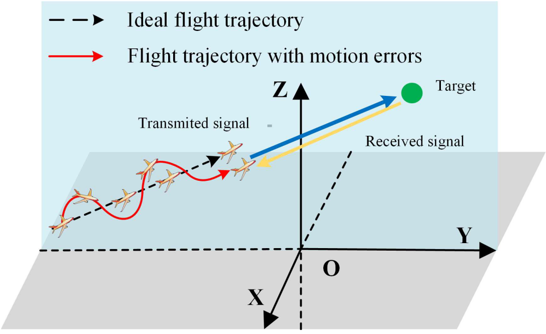

FIGURE 1. Geometrical schematic of airborne radar with motion errors.

where B is the signal bandwidth, $\lambda = c/f_c$ the signal wavelength, and A the amplitude of the pulse-compressed signal.

In practice, the airborne radar platform is subject to motion errors [23], as illustrated in Fig. 1. Motion errors lead to a significant degradation in radar system coherent integration performance, hindering target detection.

Three classical equivalent models for motion errors include linear error, quadratic error, and sinusoidal error [22–25]. The linear and quadratic errors are equivalent to the changes in the relative velocity and acceleration between the airborne radar and the target. These errors do not affect the RM and DFM correction processes in existing LTCI methods. Therefore, the radial distance between the target and the radar can be expressed as follows [23]

$$R(t_m) = R_0 + v_0 t_m + \frac{1}{2}at_m^2 + A_e\sin\left(2\pi f_e t_m\right), \tag{4}$$

where v_0 denotes the equivalent velocity when linear error exists, and a denotes the equivalent acceleration when quadratic error exists. A_e and f_e represent the amplitude and frequency of sinusoidal error, respectively.

Substituting (4) into (3), the result is given by

$$S_p(t, t_m) = A\text{sinc}\left\langle B\left\{t - \frac{2\left[R_0 + v_0 t_m + \frac{1}{2}at_m^2 + A_e\sin\left(2\pi f_e t_m\right)\right]}{c}\right\}\right\rangle \times \exp\left\{-\text{j}\frac{4\pi}{\lambda}\left[R_0 + v_0 t_m + \frac{1}{2}at_m^2 + A_e\sin\left(2\pi f_e t_m\right)\right]\right\}. \tag{5}$$

Equation (5) shows that after PC, the target's envelope varies with slow time, while the Doppler frequency variation induced by acceleration and sinusoidal error causes DFM. When RM and DFM exceed one resolution cell, range cell migration (RCM) and Doppler frequency cell migration (DFCM) occurs, degrading coherent integration performance.

In (5), $at_m^2/2$ represents the RM affected by acceleration. Assuming a range cell size of 5 m and a coherent processing interval (CPI) of 100 ms, the relative movement distance must exceed 5 m for RCM induced by acceleration to occur. This requires an equivalent acceleration of at least 500 m/s^2. Given that such high acceleration is uncommon in practice, the RM induced by target acceleration can be considered negligible.

The following presents an analysis of RM and DFM caused by sinusoidal error. In (5), the radial range and Doppler frequency affected by the sinusoidal error are given by

$$R_s\left(t_m\right) = A_e \sin\left(2\pi f_e t_m\right), \tag{6}$$

$$f_{ds}(t_m) = -\frac{2}{\lambda}\left[2\pi A_e f_e \cos\left(2\pi f_e t_m\right)\right]. \tag{7}$$

The RCM and DFCM induced by sinusoidal error occur when the following condition is satisfied

$$\left|\max\left[R_s\left(t_m\right)\right] - \min\left[R_s\left(t_m\right)\right]\right| \approx 2|A_e| > \Delta R_c, \tag{8}$$

$$\left|\max\left[f_{ds}(t_m)\right] - \min\left[f_{ds}(t_m)\right]\right| \approx \frac{8\pi|A_e f_e|}{\lambda} > \Delta f_d, \tag{9}$$

where ΔR_c denotes the size of the range cell, and Δf_d denotes the size of the Doppler frequency cell.

Furthermore, parameter A_e typically lies within the range of $[-1, 1]$ [22], indicating that sinusoidal motion error does not significantly contribute to RM in the received echoes. However, $8\pi|A_e f_e|/\lambda$ can be much larger than a Doppler resolution cell, meaning that its impact on coherent integration cannot be ignored. Therefore, (5) can be rewritten as

$$\begin{aligned} S_p\left(t, t_m\right) =& A\text{sinc}\left\{B\left[t - \frac{2\left(R_0 + v_0 t_m\right)}{c}\right]\right\} \\ &\times \exp\left[-\mathrm{j}\frac{4\pi}{\lambda}\left(R_0 + v_0 t_m + \frac{1}{2}a t_m^2\right)\right] \\ &\times \exp\left[-\mathrm{j}\frac{4\pi}{\lambda}A_e \sin\left(2\pi f_e t_m\right)\right]. \end{aligned} \tag{10}$$

Performing the fast Fourier transform (FFT) on (10) with respect to t, the result is given by

$$\begin{aligned} S_p\left(f, t_m\right) =& A_0 \text{rect}\left(\frac{f}{B}\right)\exp\left[-\mathrm{j}\frac{4\pi f}{c}\left(R_0 + v_0 t_m\right)\right] \\ &\times \exp\left[-\mathrm{j}\frac{4\pi}{\lambda}\left(R_0 + v_0 t_m + \frac{1}{2}a t_m^2\right)\right] \\ &\times \exp\left[-\mathrm{j}\frac{4\pi}{\lambda}A_e \sin\left(2\pi f_e t_m\right)\right], \end{aligned} \tag{11}$$

where f denotes the range frequency, and A denotes the amplitude after FFT with respect to t.

3. PRINCIPLE OF SAF-SFT-SRAF

In this section, SAF-SFT-SRAF is introduced to correct RM and DFM for coherent integration.

3.1. Range and Velocity Estimation

The principle of the first SAF-SFT operation can be expressed as

$$S_1\left(t_n, f_{t_m}\right) = \text{IFFT}_{f_n}\left\langle \text{add}_f\left\{\text{SFT}_{t_m}\left[R_1\left(f, f_n, t_m\right)\right]\right\}\right\rangle, \tag{12}$$

where $\text{add}_f\{\cdot\}$ represents the addition operation with respect to f; f_n denotes a lag-frequency variable with respect to f; $\text{IFFT}_{f_n}\langle\cdot\rangle$ denotes the inverse FFT (IFFT) with respect to f_n; t_n denotes the time variable with respect to f_n; $R_1(f, f_n, t_m)$ is a symmetric autocorrelation function (SAF) expressed as

$$R_1\left(f, f_n, t_m\right) = S_p\left(f + f_n, t_m\right) S_p^*\left(f - f_n, t_m\right). \tag{13}$$

$\text{SFT}_{t_m}[\cdot]$ represents the scaled Fourier transform (SFT) with respect to t_m, which can be expressed as

$$R_S(f, f_n, f_{t_m}) = \int R_1\left(f, f_n, t_m\right)\exp\left(-\mathrm{j}2\pi f_{t_m}\frac{t_m f_n}{h}\right)\mathrm{d}t_m, \tag{14}$$

where f_{t_m} denotes the frequency variable associated with t_m, and h is a scaling factor, typically set to 1 [11, 13].

Substituting (11) into (12) yields

$$S_1\left(t_n, f_{t_m}\right) = A_1\delta\left(t_n - \frac{4R_0}{c}\right)\delta\left(f_{t_m} + \frac{4hv_0}{c}\right), \tag{15}$$

where A_1 denotes the signal amplitude resulting from the first SAF-SFT operation.

The result contains a unique peak at $(4R_0/c, -4hv_0/c)$, allowing the range and velocity to be estimated via peak detection. Based on the estimated velocity $\hat{v}$, a phase compensation function $\exp(\mathrm{j}4\pi f\hat{v}/c)$ is constructed to compensate the RM caused by velocity in (11). When $\hat{v} = v_0$, the result is given by

$$\begin{aligned} S_p'\left(f, t_m\right) =& A_0\text{rect}\left(\frac{f}{B}\right)\exp\left(-\mathrm{j}\frac{4\pi f}{c}R_0\right) \\ &\times \exp\left[-\mathrm{j}\frac{4\pi}{\lambda}\left(R_0 + v_0 t_m + \frac{1}{2}a t_m^2\right)\right] \\ &\times \exp\left[-\mathrm{j}\frac{4\pi}{\lambda}A_e \sin\left(2\pi f_e t_m\right)\right]. \end{aligned} \tag{16}$$

Performing the IFFT on (16) with respect to f yields

$$\begin{aligned} S_p'\left(t, t_m\right) =& A\text{sinc}\left[B\left(t - \frac{2R_0}{c}\right)\right] \\ &\times \exp\left[-\mathrm{j}\frac{4\pi}{\lambda}\left(R_0 + v_0 t_m + \frac{1}{2}a t_m^2\right)\right] \\ &\times \exp\left[-\mathrm{j}\frac{4\pi}{\lambda}A_e \sin\left(2\pi f_e t_m\right)\right]. \end{aligned} \tag{17}$$

As observed from (17), the RM has been effectively corrected. However, the DFM induced by sinusoidal error and acceleration remains.

3.2. Sinusoidal Error Estimation

After RM correction, the target signal extracted along the range cell based on eatimation of $\widehat{R_0}$ can be expressed as

$$\begin{aligned} S_{\text{ext}}\left(t'_m\right) &= S'_p\left(t,t_m\right)\big|_{t=2R_0/c} \\ &= A_2\exp\left[-\mathrm{j}\,\frac{4\pi}{\lambda}\left(v_0t_m+\frac{1}{2}\,at_m^2\right)\right] \\ &\quad\times\exp\left[-\mathrm{j}\,\frac{4\pi}{\lambda}\,A_e\sin\left(2\pi f_et_m\right)\right], \end{aligned} \tag{18}$$

where $A_2 = A\exp\left(-j4\pi R_0/\lambda\right)$.

If the second SAF-SFT operation is directly applied to estimate acceleration at this stage, the phase factor related to the sinusoidal error will cause the spectrum of the result to broaden significantly, preventing energy from being concentrated. To solve this problem, this paper proposes an SRAF, which can be expressed as

$$S_{\text{SRAF}}\left(t_m\right) = S_{\text{ext}}\left(t_m\right)S^*_{\text{ext}}\left(-t_m\right). \tag{19}$$

Substituting (18) into (19) yields

$$S_{\text{SRAF}}\left(t_m\right)=A_2^2\exp\left\{-\mathrm{j}\,\frac{8\pi}{\lambda}\left[v_0t_m+A_e\sin\left(2\pi f_et_m\right)\right]\right\}. \tag{20}$$

A phase compensation function is constructed and multiplied with (20), which can be expressed as

$$H_2(A_t,f_t) = \exp\left[\mathrm{j}\,\frac{8\pi}{\lambda}\,A_t\sin\left(2\pi f_tt'_m\right)\right]. \tag{21}$$

where A_t and f_t denote the search amplitude and frequency of the sinusoidal error, respectively.

The result is then given by

$$\begin{aligned} S_{\text{SRAF}}\left(t_m;A_{\text{test}},f_{\text{test}}\right) &= A_2^2\exp\left(-\mathrm{j}\,\frac{8\pi}{\lambda}\,v_0t_m\right) \\ &\quad\times\exp\left[-\mathrm{j}\,\frac{8\pi}{\lambda}\,A_e\sin\left(2\pi f_et_m\right)\right] \\ &\quad\times\exp\left[\mathrm{j}\,\frac{8\pi}{\lambda}\,A_{\text{test}}\sin\left(2\pi f_{\text{test}}t_m\right)\right]. \end{aligned} \tag{22}$$

When $A_{\text{test}} = A_e$ and $f_{\text{test}} = f_e$, performing the FFT on (22) with respect to t_m results in the concentration of signal energy. The estimated sinusoidal error parameters can be expressed as

$$\left(\hat{A},\hat{f}\right) = \underset{\left(A_{\text{test}},f_{\text{test}}\right)}{\text{argmax}}\left\langle\max\left\{\text{FFT}\left[S_{\text{SRAF}}\left(t_m;A_{\text{test}},f_{\text{test}}\right)\right]\right\}\right\rangle. \tag{23}$$

where $\hat{A}$ and $\hat{f}$ denote the estimated amplitude and frequency of the sinusoidal error, respectively.

Based on the estimated parameters, a phase compensation function $\exp[\mathrm{j}4\pi\hat{A}\sin(2\pi\hat{f}t_m)/\lambda]$ is constructed to compensate the DFM caused by the sinusoidal error in (17). When $\hat{A} = A_e$ and $\hat{f} = f_e$, the result is given by

$$\begin{aligned} S''_p\left(t,t_m\right) &= A\text{sinc}\left[B\left(t-\frac{2R_0}{c}\right)\right] \\ &\quad\times\exp\left[-\mathrm{j}\,\frac{4\pi}{\lambda}\left(R_0+v_0t_m+\frac{1}{2}\,at_m^2\right)\right]. \end{aligned} \tag{24}$$

As observed from (24), the DFM caused by sinusoidal error has been effectively corrected. However, the DFM induced by acceleration remains.

3.3. Acceleration Estimation

After applying the sinusoidal error correction, (18) is given by

$$S'_{\text{ext}}\left(t_m\right) = A_2\exp\left[-\mathrm{j}\,\frac{4\pi}{\lambda}\left(v_0t_m+\frac{1}{2}\,at_m^2\right)\right]. \tag{25}$$

The principle of the second SAF-SFT operation can be expressed as

$$\begin{aligned} S_2\left(f_{t_m},f_\tau\right) &= \text{FFT}_\tau\left[\int R_2\left(t_m,\tau\right)\right. \\ &\quad\left.\exp\left(-\mathrm{j}\,2\pi f_{t_m}\,\frac{\tau t_m}{h}\right)\mathrm{d}t_m\right], \end{aligned} \tag{26}$$

where τ is a lag-time variable with respect to t_m; f_τ is the frequency with respect to τ; h is a scaling factor, typically set to 1 [11, 13]; $R_2(t_m,\tau)$ is another SAF, expressed as

$$R_2\left(t_m,\tau\right) = S'_{\text{ext}}\left(t_m+\tau\right)S'^*_{\text{ext}}\left(t_m-\tau\right). \tag{27}$$

Substituting (25) and (27) into (26) yields

$$S_2\left(f_{t_m},f_\tau\right) = A_3\delta\left(f_{t_m}+\frac{4ah}{\lambda}\right)\delta\left(f_\tau+\frac{4v_0}{\lambda}\right), \tag{28}$$

where A_3 denotes the signal amplitude resulting from the second SAF-SFT operation.

The result contains a unique peak at $(-4v_0/\lambda, -4ah/\lambda)$, allowing the acceleration to be estimated via peak detection. Based on the estimated acceleration $\hat{a}$, a phase compensation function $\exp(\mathrm{j}2\pi\hat{a}t_m^2/\lambda)$ is constructed to compensate the DFM caused by acceleration in (24). When $\hat{a} = a$, the result is given by

$$\begin{aligned} S'''_p\left(t,t_m\right) &= A\text{sinc}\left[B\left(t-\frac{2R_0}{c}\right)\right] \\ &\quad\exp\left[-\mathrm{j}\,\frac{4\pi}{\lambda}\left(R_0+v_0t_m\right)\right]. \end{aligned} \tag{29}$$

Ultimately, the RM and DFM induced by the velocity and acceleration, as well as motion errors of the airborne radar, are fully corrected. The flowchart of the proposed SAF-SFT-SRAF method is shown in Fig. 2.

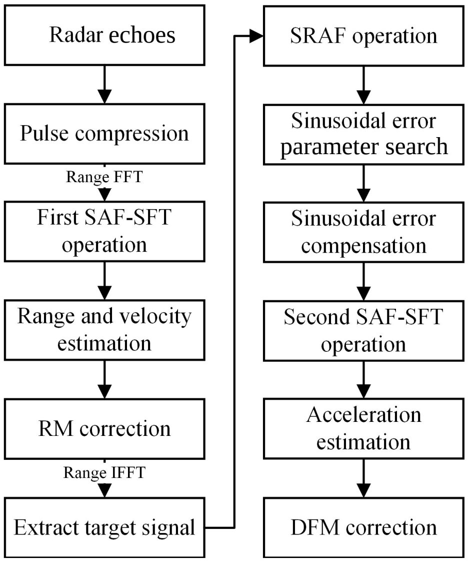

FIGURE 2. Flowchart of SAF-SFT-SRAF based method.

3.4. Cross-Terms Analysis

For multiple targets, cross-terms between echo signals may degrade the method's performance. A detailed analysis of cross-terms in the SAF-SFT method has been provided in [11] and will not be repeated here. Since this paper introduces the SRAF operation for sinusoidal error compensation, the following section focuses on cross-terms in the SRAF operation.

When multiple targets exist within the same range cell, (18) can be rewritten as

$$S_{\text{ext}}(t_m) = \sum_{i=1}^{k} A_{2i} \exp\left\{-\mathrm{j}\frac{4\pi}{\lambda}\left[v_{0i}t_m + \frac{1}{2}a_i t_m^2\right]\right\} \times \exp\left[-\mathrm{j}\frac{4\pi}{\lambda}A_e \sin(2\pi f_e t_m)\right], \tag{30}$$

where A_{2i} denotes the signal amplitude of the ith target, and a total of k targets are considered.

Applying the SRAF operation to (30), the resulting cross-terms can be expressed as

$$R_c(t_m) = \sum_{p=1}^{k}\sum_{q=1,q\neq p}^{k} A_{2p}A_{2q} \exp\left[-\mathrm{j}\frac{4\pi}{\lambda}(v_{0p}+v_{0q})t_m\right] \times \exp\left[-\mathrm{j}\frac{4\pi}{\lambda}(a_{0p}-a_{0q})t_m^2\right] \times \exp\left[-\mathrm{j}\frac{8\pi}{\lambda}A_e \sin(2\pi f_e t_m)\right]. \tag{31}$$

In (31), since $\exp[-j4\pi(a_{0p}-a_{0q})t_m^2/\lambda]$ introduces additional DFM, the cross-terms are suppressed during the sinusoidal error parameter search, preventing full energy concentration. Moreover, even if multiple targets have the same acceleration, the energy remains concentrated at the sinusoidal error amplitude A_e and frequency f_e during the search process. Therefore, SRAF effectively mitigates cross-terms interference among different targets.

4. SIMULATION RESULTS

In this section, the effectiveness of the proposed method is evaluated through computer simulations.

4.1. Coherent Integration for a Single Target

Example 1. A high-speed maneuvering target is considered, and its equivalent motion parameters are set as follows: an initial range cell number of 300, a velocity of 750 m/s, and an acceleration of 50 m/s^2. Radar parameters are set as follows: a carrier frequency of 10 GHz, a bandwidth of 10 MHz, a sample frequency of 20 MHz, a pulse repetition frequency of 10 kHz, a pulse duration of 10 µs, and a pulse number of 2048. Sinusoidal error parameters are set as follows: an amplitude of 0.8 and a frequency of 25 Hz.

The simulated signal had an SNR of 6 dB after PC. As shown in Fig. 3(a), significant RM can be observed in the echo signals. The simulation results of the proposed SAF-SFT-SRAF method are shown in Figs. 3(b)–(d). After applying RM and DFM correction, effective coherent integration is achieved. The coherent integration results before and after correction are shown in Figs. 3(e)–(f). It can be observed that, after RM and DFM correction using the proposed method, the SNR is significantly improved.

4.2. Coherent Integration for Multiple Targets

Example 2. Two high-speed maneuvering targets (Target A and Target B) are considered, with the following equivalent motion parameters: an initial range cell number of 300, a velocity of 750 m/s, and an acceleration of 50 m/s^2 for Target A; an initial range cell number of 300, a velocity of 750 m/s and an acceleration of 20 m/s^2 for Target B. The radar and sinusoidal error parameters are the same as those in Example 1.

After PC, the simulated signals for both targets had an SNR of 6 dB, as presented in Fig. 4(a). Due to the similarity in their motion parameters, the trajectories of the targets were closely clustered. The simulation results of the proposed SAF-SFT-SRAF method are illustrated in Figs. 4(b)–(d). As shown in Fig. 4(c), the sinusoidal error parameter search result still exhibits a single peak, demonstrating that the SRAF operation effectively suppresses cross-terms interference. Furthermore, Fig. 4(d) shows that the target energy is concentrated into two distinct peaks, which enhances target detection.

4.3. Computational Complexity

GRFT, IGRFT, SRT-SGRFT, and SAF-SFT methods are selected as comparison methods in this paper. Denote the numbers of pulse number, range cells, search velocities, search accelerations, search sinusoidal error amplitudes and frequencies by M, N, N_v, N_a, N_A, and N_f, respectively.

GRFT requires a three-dimensional search, while IGRFT involves a five-dimensional search, with complexities denoted as $O(N_vN_aMN)$ and $O(N_vN_aN_AN_fMN)$, respectively. Additionally, SRT-SGRFT combines the SRT operation and two SGRFT operations, with computational complexities of $O(2MN\log_2 N)$, $O(N_aMN)$, and $O(N_vN_AN_fM)$.

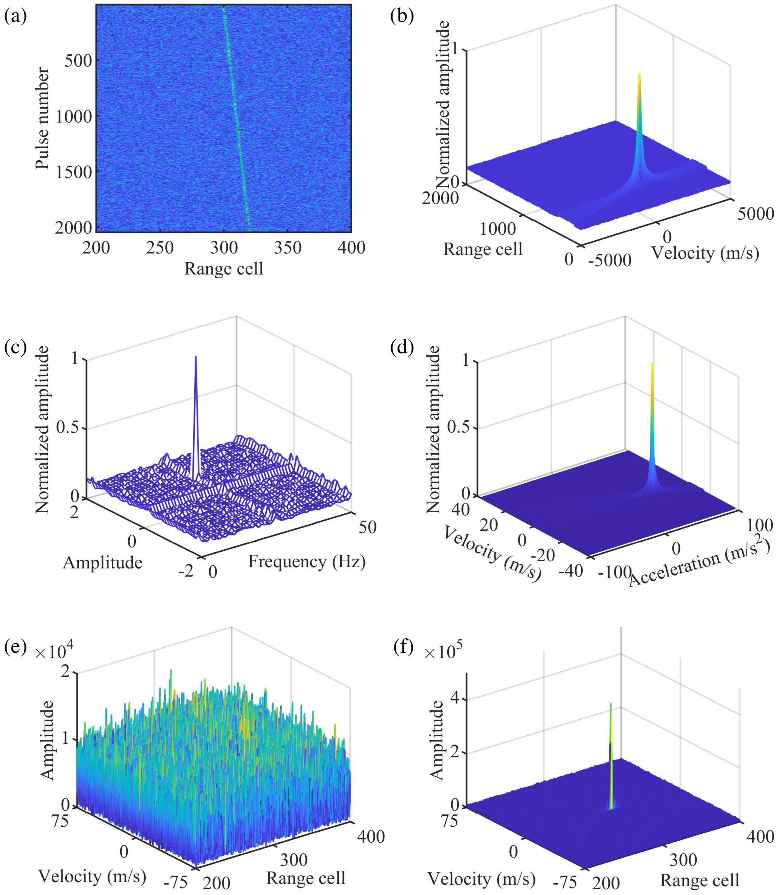

FIGURE 3. Simulation results of the SAF-SFT-SRAF method. (a) Result after PC. (b) Range-velocity estimation result. (c) Sinusoidal error parameter search result. (d) Acceleration estimation result. (e) Coherent integration result before correction. (f) Coherent integration result after correction.

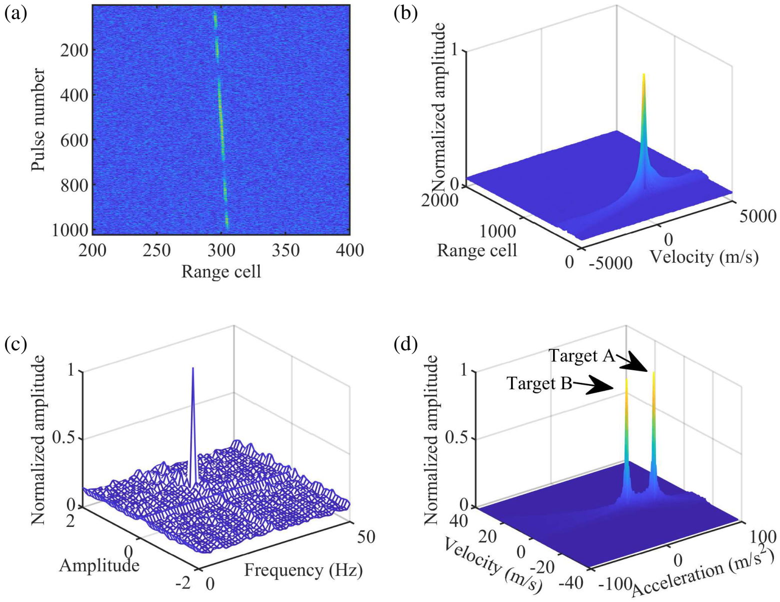

FIGURE 4. Simulation results of the SAF-SFT-SRAF method for multiple targets. (a) Result after PC. (b) Range-velocity estimation result. (c) Sinusoidal error parameter search result. (d) Acceleration estimation result.

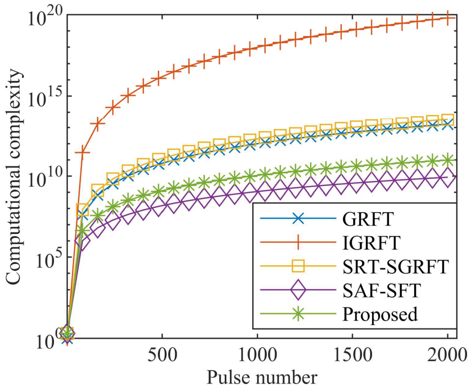

FIGURE 5. Computational complexity of each method.

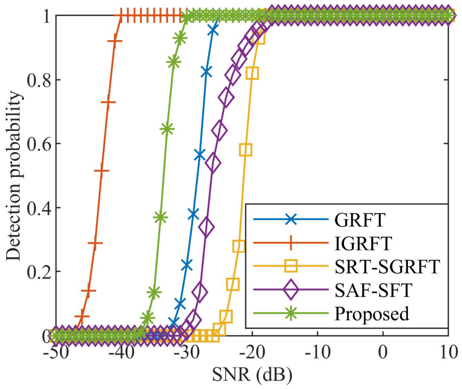

FIGURE 6. Detection probability of each method.

For the proposed SAF-SFT-SRAF method, the computational complexities of SAF-SFT, SRAF, and sinusoidal error parameter search are $O(M^3 + 6MN \log_2 M + 2MN \log_2 N)$, $O(M)$, and $O(N_A N_f M \log_2 M)$, respectively.

Assuming $N_v = N_a = N_A = N_f = N = M$, the computational complexity of each method under different pulse numbers is shown in Fig. 5. As shown in Fig. 5, GRFT, IGRFT, and SRT-SGRFT methods involve multidimensional searches, leading to high computational complexity. In contrast, the proposed SAF-SFT-SRAF method reduces the search dimensions by focusing solely on sinusoidal error parameters. Consequently, the proposed method has significantly lower computational complexity than IGRFT and SRT-SGRFT methods. However, compared to the SAF-SFT method without any search, the computational complexity of the proposed method is slightly higher.

4.4. Detection Probability

To evaluate the detection probability under noisy conditions, a constant false alarm rate (CFAR) detector is applied to each method. The SNR ranges from -50 dB to 10 dB, with 300 Monte Carlo simulations performed for each condition. Under the false alarm probability of 10^{-6}, the detection probabilities of each method as a function of SNR are shown in Fig. 6. As illustrated in Fig. 6, for the same detection probability $P_d = 0.9$, the proposed method achieves improvements of 5 dB, 1 dB, and 12 dB compared to the GRFT, SAF-SFT, and SRT-SGRFT methods, respectively. Although the detection probability of the proposed method is approximately 10 dB lower than that of the IGRFT method, its computational complexity is significantly lower.

5. CONCLUSION

To address the excessive computational complexity of existing airborne coherent integration methods, we improve the SAF-SFT method and propose the SAF-SFT-SRAF method. First, we derive the theoretical principles of the SAF-SFT-SRAF method for correcting RM and DFM. The effectiveness of the proposed method is then verified through simulations. Finally, we compare the proposed method with several representative coherent integration methods in terms of computational complexity and detection probability, demonstrating its advantages in practical applications. However, the iterative compensation strategy employed in the proposed method is susceptible to error propagation, and the SRAF operation amplifies the noise level, leading to poor anti-noise performance in sinusoidal error parameter search, potentially compromising the accuracy of subsequent acceleration estimation. In future work, the idea of simultaneously estimating multiple parameters using IGRFT may be referred to in order to further improve the proposed method.

ACKNOWLEDGEMENT

This work was supported in part by the China Postdoctoral Foundation (2023M731680) and Youth Foundation of Jiangsu Province (BK20230919).

REFERENCES

[1] Jin, K., G. Li, T. Lai, T. Jin, and Y. Zhao, "A novel long-time coherent integration algorithm for Doppler-ambiguous radar maneuvering target detection," *IEEE Sensors Journal*, Vol. 20, No. 16, 9394–9407, Aug. 2020.

[2] Lin, L., G. Sun, Z. Cheng, and Z. He, "Long-time coherent integration for maneuvering target detection based on ITRT-MRFT," *IEEE Sensors Journal*, Vol. 20, No. 7, 3718–3731, Apr. 2020.

[3] Wang, H., W. Huang, H. Zhang, T. Ba, and Z. Yang, "Modified adaptive RFT with sample covariance matrix inversion recursive estimation," *Progress In Electromagnetics Research C*, Vol. 145, 181–187, 2024.

[4] Kirkland, D. M., "An alternative range migration correction algorithm for focusing moving targets," *Progress In Electromagnetics Research*, Vol. 131, 227–241, 2012.

[5] Huang, P., G. Liao, Z. Yang, X.-G. Xia, J.-T. Ma, and J. Ma, "Long-time coherent integration for weak maneuvering target detection and high-order motion parameter estimation based on keystone transform," *IEEE Transactions on Signal Processing*, Vol. 64, No. 15, 4013–4026, Aug. 2016.

[6] Li, S., Y. Wang, B. Wang, G. Battistelli, L. Chisci, and G. Cui, "Efficient dual-scale generalized Radon-Fourier transform detector family for long time coherent integration," *IEEE Transactions on Signal Processing*, Vol. 72, 4237–4252, 2024.

[7] Pu, W., J. Wu, Y.-L. Huang, X.-D. Wang, J.-Y. Yang, W.-C. Li, and H.-G. Yang, "Nonsystematic range cell migration analy-

sis and autofocus correction for bistatic forward-looking SAR," *IEEE Transactions on Geoscience and Remote Sensing*, Vol. 56, No. 11, 6556–6570, Nov. 2018.

[8] Chen, J., M. Xing, H. Yu, B. Liang, J. Peng, and G.-C. Sun, "Motion compensation/autofocus in airborne synthetic aperture radar: A review," *IEEE Geoscience and Remote Sensing Magazine*, Vol. 10, No. 1, 185–206, Mar. 2022.

[9] Zhang, S.-S., T. Zeng, T. Long, and H.-P. Yuan, "Dim target detection based on keystone transform," in *IEEE International Radar Conference*, 889–894, Arlington, VA, USA, 2005.

[10] Zheng, J., T. Su, W. Zhu, X. He, and Q. H. Liu, "Radar high-speed target detection based on the scaled inverse Fourier transform," *IEEE Journal of Selected Topics in Applied Earth Observations and Remote Sensing*, Vol. 8, No. 3, 1108–1119, Mar. 2015.

[11] Li, X., Z. Sun, W. Yi, G. Cui, L. Kong, and X. Yang, "Computationally efficient coherent detection and parameter estimation algorithm for maneuvering target," *Signal Processing*, Vol. 155, 130–142, 2019.

[12] Huang, P., G. Liao, Z. Yang, X.-G. Xia, J.-T. Ma, and X. Zhang, "A fast SAR imaging method for ground moving target using a second-order WVD transform," *IEEE Transactions on Geoscience and Remote Sensing*, Vol. 54, No. 4, 1940–1956, Apr. 2016.

[13] Lv, X., G. Bi, C. Wan, and M. Xing, "Lv's distribution: Principle, implementation, properties, and performance," *IEEE Transactions on Signal Processing*, Vol. 59, No. 8, 3576–3591, Aug. 2011.

[14] Li, D., M. Zhan, J. Su, H. Liu, X. Zhang, and G. Liao, "Performances analysis of coherently integrated CPF for LFM signal under low SNR and its application to ground moving target imaging," *IEEE Transactions on Geoscience and Remote Sensing*, Vol. 55, No. 11, 6402–6419, Nov. 2017.

[15] Zheng, J., H. Liu, J. Liu, X. Du, and Q. H. Liu, "Radar high-speed maneuvering target detection based on three-dimensional scaled transform," *IEEE Journal of Selected Topics in Applied Earth Observations and Remote Sensing*, Vol. 11, No. 8, 2821–2833, Aug. 2018.

[16] Zhao, L., H. Tao, and W. Chen, "Maneuvering target detection based on three-dimensional coherent integration," *IEEE Access*, Vol. 8, 188 321–188 334, 2020.

[17] Xu, J., X.-G. Xia, S.-B. Peng, J. Yu, Y.-N. Peng, and L.-C. Qian, "Radar maneuvering target motion estimation based on generalized Radon-Fourier transform," *IEEE Transactions on Signal Processing*, Vol. 60, No. 12, 6190–6201, Dec. 2012.

[18] Yang, M., D. Zhu, and W. Song, "Comparison of two-step and one-step motion compensation algorithms for airborne synthetic aperture radar," *Electronics Letters*, Vol. 51, No. 14, 1108–1110, 2015.

[19] Ribalta, A., "One-step motion compensation algorithm for squinted SAR," in *2016 IEEE International Geoscience and Remote Sensing Symposium (IGARSS)*, 1154–1157, Beijing, China, 2016.

[20] Li, J., J. Chen, P. Wang, and O. Loffeld, "A coarse-to-fine autofocus approach for very high-resolution airborne stripmap SAR imagery," *IEEE Transactions on Geoscience and Remote Sensing*, Vol. 56, No. 7, 3814–3829, Jul. 2018.

[21] Pu, W., J. Wu, Y. Huang, J. Yang, and H. Yang, "Fast factorized backprojection imaging algorithm integrated with motion trajectory estimation for bistatic forward-looking SAR," *IEEE Journal of Selected Topics in Applied Earth Observations and Remote Sensing*, Vol. 12, No. 10, 3949–3965, Oct. 2019.

[22] Wu, J., "Research on high-speed moving target integration detection method of airborne radar," M.S. thesis, Univ. Electron. Sci. Technol. China, Chengdu, China, 2022.

[23] Yang, F., X. Li, M. Wang, Z. Sun, and G. Cui, "IGRFT-based signal coherent integration method for high-speed target with airborne bistatic radar," in *2022 16th IEEE International Conference on Signal Processing (ICSP)*, Vol. 1, 529–534, Beijing, China, 2022.

[24] Pu, W., J. Wu, Y. Huang, K. Du, W. Li, J. Yang, and H. Yang, "A rise-dimensional modeling and estimation method for flight trajectory error in bistatic forward-looking SAR," *IEEE Journal of Selected Topics in Applied Earth Observations and Remote Sensing*, Vol. 10, No. 11, 5001–5015, Nov. 2017.

[25] Wang, Y., Z. Wang, B. Zhao, and L. Xu, "Compensation for high-frequency vibration of platform in SAR imaging based on adaptive chirplet decomposition," *IEEE Geoscience and Remote Sensing Letters*, Vol. 13, No. 6, 792–795, Jun. 2016.